JOURNAL OF COMPUTATIONAL PHYSICS 69, 362–396 (1987)

Higher-Order Accurate Difference Solutions of Vortex Generation from a Circular Cylinder in an Oscillatory Flow

NOBUHIRO BABA AND HIDEAKI MIYATA

Department of Naval Architecture, University of Tokyo, Tokyo, Japan

Received December 31, 1985; revised June 2, 1986

A higher-order difference solution method is presented for viscous flow around an oscillating body. The Navier–Stokes equation in a rotational form, which conserves both momentum and kinetic energy, is approximated into a difference form by a fourth-order compact differencing in a general boundary-fitted curvilinear coordinate system. A time-marching procedure is derived and the high resolution property is demonstrated with the computations of some simple problems. The simulation of a viscous flow around a circular cylinder sinusoidally oscillating at low Keulegan–Carpenter number elucidates fairly well the sequential viscous flow mechanism of boundary layer development, flow separation, and vortex shedding with pairing.

CONTENTS.

1. INTRODUCTION

Unsteady vortical flow around a circular cylinder has long been of interest both experimentally and theoretically. It contains a lot of very nonlinear mechanics such as flow separation, vortex shedding, and turbulence. Continuous efforts have been devoted for the thorough understanding of the nonlinear flow mechanics around a circular cylinder and it is going to be noted that numerical experiments will be useful for this purpose. In the field of ocean engineering, in particular, vortex shedding from a circular cylinder in an oscillatory flow is of significant importance. Ocean waves generate oscillatory flows around a member of an offshore structure or a vertical riser pipe, and they induce in-line and transverse forces due to unsymmetric vortex shedding. Resonant oscillations caused by these forces may destroy riser pipes of an oil production system in ocean.

The in-line and transverse forces are generated by complicated vortex shedding

0021-9991/87 $3.00

motions and depend on both Reynolds number $\mathrm{Re} = V_m d/\nu$ and Keulegan–Carpenter number $Kc = V_m T/d$, where V_m is amplitude of oscillatory flow velocity, d diameter of a circular cylinder, ν kinematic viscosity, and T period of oscillation. The estimation of these forces has been mostly based on empirical equations derived from laboratory experiments of force measurement [14]. The detailed mechanism of generating these forces is not well elucidated, since the vortex motions are quite complicated and they show a variety of pairing patterns at different Kc numbers as observed, for example, by Williamson [19].

A lot of numerical studies have been focused on the problem of vortex shedding from an impulsively started circular cylinder. Most successful examples seem to be those by Loc [8] and Badr and Dennis [1], in which vorticity-streamfunction equations are numerically solved with particular techniques. However, these approaches seem to find difficulties in extending to three-dimensional cases with obstacles of arbitrary three-dimensional configuration and to higher Reynolds number cases by incorporating subgrid-scale turbulence model.

In this study the Navier–Stokes (NS) equations are directly integrated with primitive variables, basically following the algorithm presented by Harlow and Welch [4]. The NS-equations are deformed into conservative forms, in which both momentum and kinetic energy are conserved. Since low-order truncation error contaminates the solution, adequate higher-order differencing scheme must be employed, which is essentially important for a viscous flow problem. One of the most favorable schemes is the compact finite differencing by Hirsh [5], which achieves high-order discretizations of differential equations without an enlargement of the band width of the resulting set of discrete equations.

In recent years successful simulation of ship waves were undertaken using an inflexible rectangular mesh system [11] and the averaged wave breaking motion was also simulated with this simplest coordinates [12]. However, since we must solve the flow field bounded by boundaries of arbitrary configuration, the use of a boundary-fitted coordinate system is necessary. It is of fundamental importance for the simulation of vortex generation on the body surface. Among a number of methods [17] the method based on the solution of an elliptic differential system is advantageous since a fairly smooth grid system which is easily adjustable is obtained.

In Section 2 the method of generating a boundary-fitted coordinate system is described. The derivation of the NS-equations in conservative form is explained in Section 3. The computational procedure and boundary conditions are described in Sections 4 and 5, respectively. The space differencing scheme is briefly described in Section 6. Some numerical tests to ensure the degree of accuracy of the present method are performed in Section 7 including computation of a flow around an impulsively started circular cylinder in a uniform flow. Simulations of vortex shedding in an oscillatory flow at $Kc = 5$ and 7 are presented and discussed in Section 8. Brief concluding remarks are mentioned in Section 9.

2. GENERATION OF BOUNDARY-FITTED COORDINATE SYSTEM

A boundary-fitted coordinate system has coordinate surfaces coincident with all boundaries of arbitrary configuration, which is not necessarily orthogonal but general curvilinear. General curvilinear coordinates ξ^i in a Euclidean space may be defined as the differentiable functions of the Cartesian coordinates x^i,

$$\xi^i = \xi^i(x^1, x^2, x^3), \qquad i = 1, 2, 3. \tag{2.1}$$

The transformation of coordinates (2.1) can always be inverted to

$$x^i = x^i(\xi^1, \xi^2, \xi^3), \qquad i = 1, 2, 3, \tag{2.2}$$

provided that the transformation matrix

$$T^i_j = \frac{\partial x^i}{\partial \xi^j} \tag{2.3}$$

is non singular, which means that the Jacobian

$$J = \det(T^i_j) \tag{2.4}$$

exists and does not vanish. Let E be a physical region in $x^1x^2x^3$-space bounded by arbitrary-shaped boundaries ∂E and R be a rectangular transformed region in $\xi^1\xi^2\xi^3$-space. Grid generation and subsequent computations are made in the transformed region R, hence the metric tensor g_{ij} is given by

$$g_{ij} = T^k_i T^l_j \delta_{kl}, \tag{2.5}$$

$$g = \det(g_{ij}), \tag{2.6}$$

$$g^{ij} = \tfrac{1}{2} g^{-1} e^{imn} e^{jpq} g_{mp} g_{nq}, \tag{2.7}$$

where δ and e denote the Kronecker delta and the Eddington permutation symbol, respectively.

The problem of grid generation is to find the smooth functions of Eq. (2.2) in R when the shape of the boundaries ∂E is given by Cartesian coordinates. The method to let the coordinates be solutions of an elliptic partial differential system can conveniently control the coordinate spacing [16] and can cope with a time-dependent coordinate system, the use of which is requested by the free surface problems [15]. Furthermore it can be generalized to three dimensions [9]. The governing equation in the transformed region R for the boundary-fitted coordinate system is

$$g^{ij} \frac{\partial^2 x^l}{\partial \xi^i \, \partial \xi^j} + \psi^i \frac{\partial x^l}{\partial \xi^i} = 0, \tag{2.8}$$

where

$$\psi^i = \bar{A}^i \operatorname{sgn}(\bar{\xi}^i - \xi^i) \exp(-\bar{B}^i |\bar{\xi}^i - \xi^i|) \tag{2.9}$$

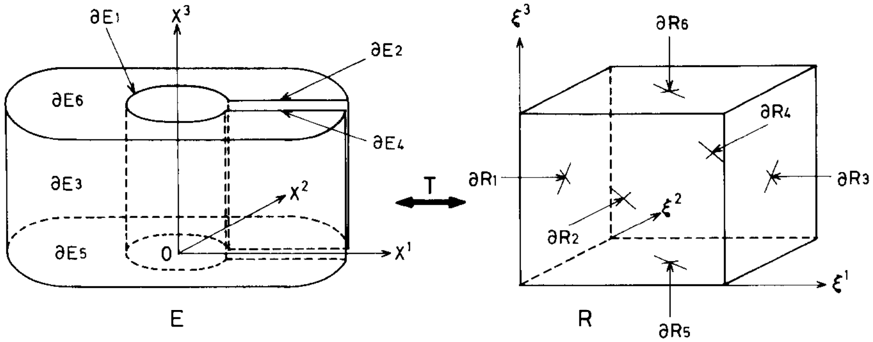

FIG. 1. Field transformation, left; physical region, right; transformed region.

plays the role of attracting the coordinate surfaces of $\xi^i = \text{const.}$ to a specified coordinate surface $\xi^i = \bar{\xi}^i$.

Appropriate boundary conditions are given to Eq. (2.8) by geometric configuration of the problem and the pattern of transformation. For our present problem of a flow around a vertical cylinder the transformation pattern shown in Fig. 1 is chosen. A doubly connected region E about a circular cylinder is transformed to a rectangular region R, with the boundaries ∂E_i of the physical region E corresponding to ∂R_i of the transformed region R for $i = 1, 2, \ldots, 6$, respectively. On the boundaries ∂R_2 and ∂R_4 which correspond to the re-entrant boundaries ∂E_2 and ∂E_4, respectively, the periodic conditions are imposed on any functions in R. Dirichlet and Neumann conditions are used on the other boundaries as follows.

$$\begin{aligned} &x^1 = \bar{x}^1, \qquad x^2 = \bar{x}^2, \qquad \frac{\partial x^3}{\partial \xi^1} = 0 \quad \text{on} \quad \partial R_1, \partial R_3, \\ &\frac{\partial x^1}{\partial \xi^3} = 0, \qquad \frac{\partial x^2}{\partial \xi^3} = 0, \qquad x^3 = \bar{x}^3 \quad \text{on} \quad \partial R_5, \partial R_6. \end{aligned} \tag{2.10}$$

The second-order centered difference scheme is used to approximate the spatial derivatives in Eqs. (2.3) and (2.8). A quasilinear elliptic differential system (2.8) is solved by a successive relaxation method.

3. GOVERNING EQUATIONS

Governing equations are written in the general curvilinear coordinates $(\xi^1\ \xi^2, \xi^3)$, since a boundary-fitted coordinate system is employed. Now consider that a circular cylinder oscillates in a viscous incompressible fluid at right angle to its axis, namely in the direction parallel to the x^1-axis (see Fig. 1). Instantaneous velocity of oscillation is given by

$$V = V_m \sin\left(\frac{2\pi}{T} t\right), \tag{3.1}$$

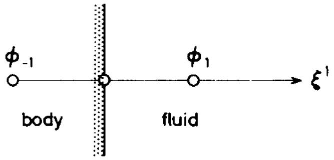

FIG. 2. Definition sketch for the extrapolation on body boundary.

where V_m is amplitude of oscillatory velocity, T period of oscillation and t time. The NS-equation for the sinusoidal flow is written as

$$Kc^{-1}\frac{\partial u^i}{\partial t} + (u^iu^j)_{;j} = -g^{ij}P_{;j} + \mathrm{Re}^{-1}g^{jk}u^i_{;jk} - 2\pi Kc^{-1}\cos(2\pi t)\, g^{ij}T^1_j, \tag{3.2}$$

$$u^i_{;i} = 0. \tag{3.3}$$

Here all the variables are made dimensionless with reference to diameter of the circular cylinder d, by amplitude of the oscillatory velocity V_m, and by period of oscillation T. Dimensionless parameters are Reynolds number $\mathrm{Re} = V_m d/\nu$ and Keulegan–Carpenter number $Kc = V_m T/d$. Primitive variables are contravariant components u^i of the flow velocity vector relative to the circular cylinder and pressure P. A subscript with (;) denotes covariant derivative. The last term in the momentum equation (3.2) represents the oscillatory acceleration in the x^1 direction, in which T^i_j is the transformation matrix defined by Eq. (2.3).

The momentum equation (3.2) is very complicated since some undifferentiated terms arise from the covariant derivatives of a vector or a tensor. For example the advective term is rewritten as

$$(u^iu^j)_{;j} = \frac{\partial}{\partial \xi^j}(u^iu^j) + \Gamma^j_{jk}u^iu^k + \Gamma^i_{jk}u^ju^k, \tag{3.4}$$

where Γ^i_{jk} is the second kind of Christoffel symbol. These additional undifferentiated terms increase the number of operations in the numerical calculation and may introduce pseudophysical errors into the computation. Warsi introduced compressible NS-equation that does not contain undifferentiated terms [18]. However, his equation does not seem to be suitable for the numerical computation of incompressible flows, since the explicit expression of stress terms is not provided. Therefore, the NS-equation must be in a compact form appropriate for the numerical computation of a viscous incompressible flow.

For this purpose, we use the NS-equation in the rotational form, in which the advective term is expressed by the kinetic energy gradient and the outer product of velocity and rotation, and the viscous stress terms by the rotation of vorticity. Since the gradient of a scalar, the divergence of a contravariant vector and the rotation of a covariant vector can be written in the compact form as

$$a_{;i} = \frac{\partial a}{\partial \xi^i}, \tag{3.5}$$

$$a^i_{;i} = g^{-1/2} \frac{\partial}{\partial \xi^i} (g^{1/2} a^i), \tag{3.6}$$

$$\varepsilon^{ijk} a_{k;j} = \varepsilon^{ijk} \frac{\partial a_k}{\partial \xi^j}. \tag{3.7}$$

The NS-equation in the rotational form becomes

$$\begin{aligned} Kc^{-1} \frac{\partial u^i}{\partial t} = {} & - g^{ij} \frac{\partial \phi}{\partial \xi^j} + g^{ij} \varepsilon_{jkl} u^k \omega^l \\ & - \mathrm{Re}^{-1} \varepsilon^{ijk} \frac{\partial}{\partial \xi^j} (g_{kl} \omega^l) \\ & - 2\pi Kc^{-1} \cos(2\pi t)\, g^{ij} T^1_j, \end{aligned} \tag{3.8}$$

$$g^{-1/2} \frac{\partial}{\partial \xi^i} (g^{1/2} u^i) = 0. \tag{3.9}$$

Here ϕ is Bernoulli scalar defined by

$$\phi = P + \tfrac{1}{2} g_{kl} u^k u^l, \tag{3.10}$$

and ω^i is a contravariant vector of vorticity as

$$\omega^i = \varepsilon^{ijk} \frac{\partial}{\partial \xi^j} (g_{kl} u^l). \tag{3.11}$$

The symbols ε^{ijk} and ε_{ijk} in Eqs. (3.7), (3.8), and (3.11) are third-order tensors and refer to Eddington permutation symbol e as

$$\varepsilon_{ijk} = g^{1/2} e_{ijk}, \qquad \varepsilon^{ijk} = g^{-1/2} e^{ijk}. \tag{3.12}$$

Equations (3.8) and (3.9) are the governing equations in the general curvilinear coordinates, and they are appropriate to the three-dimensional direct simulation in a boundary-fitted coordinate system since they do not include any additional undifferentiated terms.

Furthermore the rotational form of the NS-equation has another advantage of having the conservative property for kinetic energy as well as momentum [10]. In the viscous incompressible fluid the kinetic energy is dissipated by the viscous stresses unless it is supplied from outside. In the absence of time-differencing errors this process of energy dissipation can be simulated even if the symmetric difference schemes are used to approximate spatial derivatives.

4. COMPUTATIONAL PROCEDURE

Using forward difference in time, the momentum equation (3.8) is rewritten as

$$Kc^{-1}\frac{\overset{(n+1)}{u^{i}}}{\Delta t}+g^{ij}\frac{\partial\phi}{\partial\xi^{j}}=a^{i}, \tag{4.1}$$

where

$$\begin{aligned} a^{i}=Kc^{-1}\frac{u^{i}}{\Delta t}&+g^{ij}\varepsilon_{jkl}u^{k}\omega^{l}\\ &-\mathrm{Re}^{-1}\varepsilon^{ijk}\frac{\partial}{\partial\xi^{j}}(g_{kl}\omega^{l})\\ &-2\pi Kc^{-1}\cos(2\pi t)\,g^{ij}T_{j}^{1}. \end{aligned} \tag{4.2}$$

Here the superscript $(n+1)$ denotes the $(n+1)$th time level and (n) is dropped for simplicity. To determine the velocity vector u^i at the $(n+1)$th time-step and Bernoulli scalar ϕ, a contravariant vector a^i is decomposed into the solenoidal and irrotational vector fields as Eq. (4.1). The flow velocity vector u^i at the nth time-step is retained in the vector a^i of Eq. (4.2), since the incompressibility constraint is imposed at every time step to prevent the velocity field at the $(n+1)$th time-step from systematically accumulating numerical errors [4].

This procedure of Helmholz decomposition provides the fundamental algorithm used in the MAC-type simulation of incompressible flows [13]. By taking the divergence of Eq. (4.1) and letting the divergence at the $(n+1)$th time-step zero through Eq. (3.9), we have a Poisson equation for the Bernoulli scalar

$$\frac{\partial}{\partial\xi^{i}}\left(g^{1/2}g^{ij}\frac{\partial\phi}{\partial\xi^{j}}\right)=b, \tag{4.3}$$

where

$$b=\frac{\partial}{\partial\xi^{i}}(g^{1/2}a^{i}). \tag{4.4}$$

Equation (4.3) is solved by a successive relaxation method under boundary conditions and the irrotational field of the second term of Eq. (4.1) is calculated from the solution of ϕ. Then the solenoidal velocity field at the $(n+1)$th time step is renewed by Eq. (4.1).

5. BOUNDARY AND INITIAL CONDITIONS

The computational domain is surrounded by body boundary, open boundaries at a distance and upper and lower boundaries, on which proper treatments are necessary.

On the body boundary a no-slip condition is imposed as

$$u^i = 0. \tag{5.1}$$

Substituting Eq. (5.1) into the NS-equation (4.1), the equation for the Bernoulli scalar quantity ϕ is derived as

$$g^{ij} \frac{\partial \phi}{\partial \xi^j} = a^i. \tag{5.2}$$

Since (5.2) is a vector equation, this gives too many conditions for the scalar ϕ to be determined by the Poisson equation (4.3) [13]. Therefore, only one component of them which is approximately normal to the body surface $\xi^1 = \text{const.}$ is taken as

$$\frac{\partial \phi}{\partial \xi^1} = g_{i1} a^i. \tag{5.3}$$

Since it is assumed that the disturbance from the circular cylinder does not reach the surrounding open boundaries in the present oscillatory flow problem owing to the use of an adequately large domain of computation, the following infinity condition is used on the open boundaries far away from the circular cylinder.

$$\phi = \bar{P}_{\infty} + \tfrac{1}{2} g_{kl} u^k u^l. \tag{5.4}$$

A periodic condition is used on the upper and lower horizontal boundaries. Since the minimum number of grid point is used in the direction parallel to the axis of the cylinder, the simulation is quite two-dimensional in the present computations, although the formulation and the computer code are fully three-dimensional. However, this seems to be appropriate for low Reynolds number flows ($\mathrm{Re} \leqslant 1000$) considered in the present study.

The initial condition for the velocity which satisfies the incompressibility constraint is given by the stationary state

$$u^i = 0 \quad \text{at} \quad t = 0. \tag{5.5}$$

6. SPACE DIFFERENCING

The degree of accuracy of the difference approximation must be raised so that the truncation error does not contaminate the solution. In viscous flow problems, in particular, numerical dissipation must be carefully diminished. The truncation error of the nth order difference scheme for the mth derivative is expressed as $\Delta^n d^{n+m}/d\xi^{n+m}$. There are two ways to reduce this error and raise the spatial resolution. One is to increase n, namely, to use a higher-order scheme, and the other is to reduce grid spacing in the region where flow variables have large gradient.

In this study a relatively fine spacing is generated near the body by attracting the grid system and a fourth-order accurate compact difference scheme [5, 13] is used for the space derivatives in the calculations of vorticity in Eq. (3.11), viscous stress terms in Eq. (4.2), source terms of Eq. (4.4), and gradient of ϕ in Eq. (4.1). In the solution procedure for the pressure field by Eq. (4.3) a second-order centered differencing is used for the sake of computational economy. The compact differencing is advantageous in that it can be applied without an enlargement of the band width of the resulting set of discrete equation. Some other higher-order differencings necessitate larger numbers of points for space differencing, which makes the boundary conditions complicated. It is noted that a higher-order differencing is often susceptible to intrinsic instability. Christie [2] proposed an upwind compact difference scheme to add a favorable stabilizing property to the compact difference scheme of Hirsh [5]. However, it seems to be almost impossible for his scheme to maintain the fourth-order accuracy, since the contribution of the first-order upwind differencing may degrade the accuracy in actual cases. Therefore, the differencing method by Hirsh [5] is used here, carefully considering the stability property with Courant and diffusion numbers as parameters.

The compact difference scheme $\overset{c}{D}$ is written as

$$\overset{c}{D} = \overset{0}{D}/(1 + \Delta^2 \overset{+}{D} D/6), \tag{6.1}$$

where $\overset{0}{D}$, $\overset{+}{D}$, and D denote centered, forward, and backward difference operators, respectively. Now let I be the operator such that

$$I^n f(x) = f(x + n\Delta), \tag{6.2}$$

then, the difference operators are

$$\overset{0}{D} = (I - I^{-1})/2\Delta, \tag{6.3}$$

$$\overset{+}{D} = (I - 1)/\Delta, \tag{6.4}$$

$$D = (1 - I)/\Delta, \tag{6.5}$$

$$\overset{+}{D}\overset{-}{D} = (I - 2 + I^{-1})/\Delta^2. \tag{6.6}$$

Hence $\overset{c}{D}f\ (= f')$ becomes

$$\frac{1}{6}(I + 4 + I^{-1})\, f' = \frac{1}{2\Delta}(I - I^{-1})\, f. \tag{6.7}$$

The differential coefficient f' is simultaneously calculated along a coordinate line by the numerical solution of the tridiagonal linear system. However, for the computational efficiency the initial value of f' is predicted by the centered differencing (6.3) as

$$f'_{(0)} = \overset{0}{D}f, \tag{6.8}$$

and then an iterative calculation is made to raise the accuracy up to the fourth order through the following equations derived from Eq. (6.7).

$$f'_{(m+1)}=f'_{(m)}+\varDelta s\left\{-\frac{1}{6}(I+4+I^{-1})f'_{(m)}+\frac{1}{2\varDelta}(I-I^{-1})f\right\}. \tag{6.9}$$

The relaxation factor $\varDelta s$ is set at 0.6.

On the boundaries, except for those on which a periodic condition is applied, forward, or backward differencing is used due to the lack of velocity points outside the boundaries.

In the iterative solution procedure of the Poisson equation (4.3) for ϕ the space differencing is approximated by centered differencing as

$$\frac{\partial}{\partial\xi^i}\left(g^{1/2}g^{ij}\frac{\partial\phi}{\partial\xi^j}\right)\approx\overset{0}{D}_i(g^{1/2}g^{ij})\overset{0}{D}_j\phi+g_{1/2}g^{ij}\begin{cases}\overset{0}{D}_i\overset{0}{D}_j\phi & (i\neq j)\\ \overset{+}{D}_i\overset{-}{D}_j\phi & (i=j)\end{cases}. \tag{6.10}$$

Similarly the body boundary condition (5.3) becomes

$$\overset{0}{D}_1\phi=g_{i1}a^i. \tag{6.11}$$

For the solution of (6.11) ϕ is extrapolated outward from the interior value ϕ_1, by the following equation, see Fig. 2.

$$\phi_{-1}=\phi_1-2g_{i1}a^i\varDelta. \tag{6.12}$$

7. NUMERICAL TESTS

7.1. *Condition of Computation*

The accuracy of the present method is examined by the solution of a uniform flow problem and the effectiveness of the compact difference scheme is demonstrated by the solution of an oscillatory flow problem.

All the variables are made dimensionless in all the computations in this paper; length with respect to the unit length of the diameter of the circular cylinder d, velocity with respect to the amplitude of the oscillatory flow velocity or the steady flow velocity V_m and time with respect to d/V_m in the uniform flow case or the period of oscillation T in the oscillatory flow case. Therefore, pressure and vorticity are made dimensionless with respect to $1/2\rho V_m^2$ and V_m/d, although pressure in the formulations is made dimensionless with respect to ρV_m^2. In the case of oscillatory flow the cylinder is moved with the grid system fixed to it at the speed of Eq. (3.1). However, the flow velocities are shown with values in the coordinate system fixed to the cylinder for convenience in the figures and their captions in this paper, assuming that the cylinder is fixed and the fluid travels right and left around it.

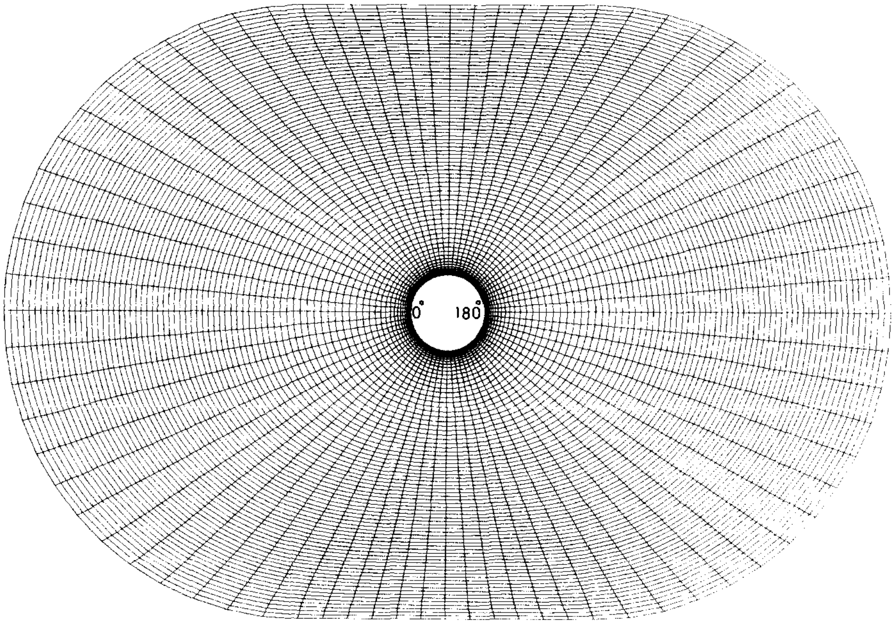

FIG. 3. Coarser grid system.

The coarser grid system shown in Fig. 3 is used for the numerical tests. The number of grid point is $78 \times 76 \times 3$ in radial, circumferential and axial directions, respectively. To raise the resolution in the proximity of the circular cylinder the coordinate surfaces are attracted onto the body surface with the factors $A = 10000$ and $B = 0.5$. The smallest space difference in the radial direction is about 0.5 percent of the diameter of the cylinder.

From the Courant condition for stability the following limitation on the time increment is derived,

$$\Delta t \leqslant \frac{\Delta x^1}{Kc\, u^1}. \tag{7.1}$$

Here u^1 is the radial velocity and Δx^1 is the smallest radial spacing. If we assume the velocity is unity on the body surface where Δx^1 is 0.005, Δt must be smaller than 0.005, since Kc is unity in the uniform flow problem.

In the computed results the velocity and vorticity components are evaluated in the Cartesian coordinates.

7.2. *Circular Cylinder in a Uniform Flow*

A circular cylinder is accelerated from at rest to the unit steady speed for unit period at Re = 1000. Since the time increment is set at 0.001 and the computation is

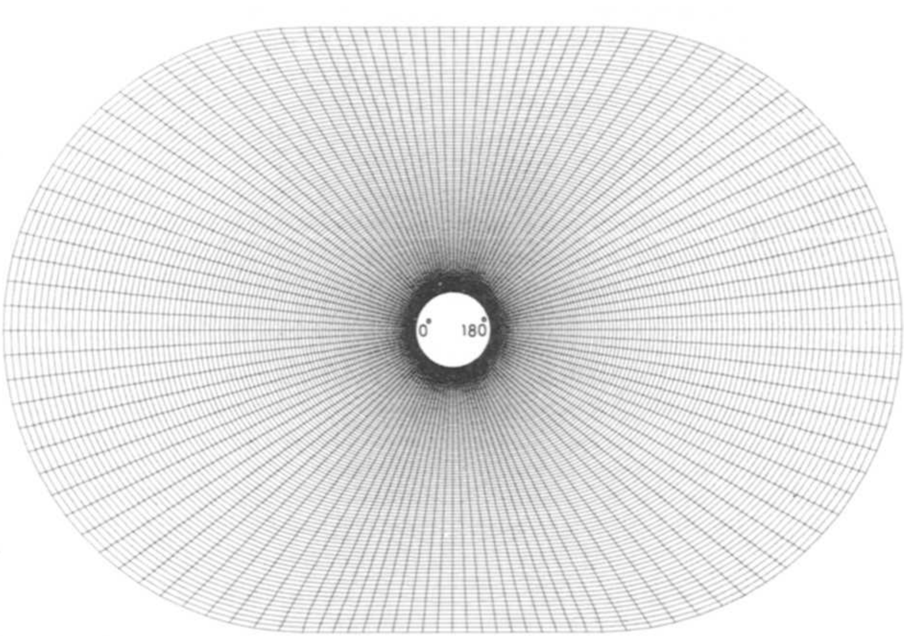

FIG. 4. Finer grid system.

continued for 3000 time-steps; the steady speed is reached at $t = 1$ and the computation is stopped at $t = 3$.

The computed velocity vector field in the vicinity of the circular cylinder at $t = 3$ is shown in Fig. 6. It is obviously noted that a secondary twin vortex is simulated near the separation point in front of the large twin vortex. This result seems to demonstrate the high resolution property of the present method, since the secondary twin vortex is a vortex of small strength that appears at the Reynolds number greater than 550 and plays an important role in the separation mechanism [6, 8].

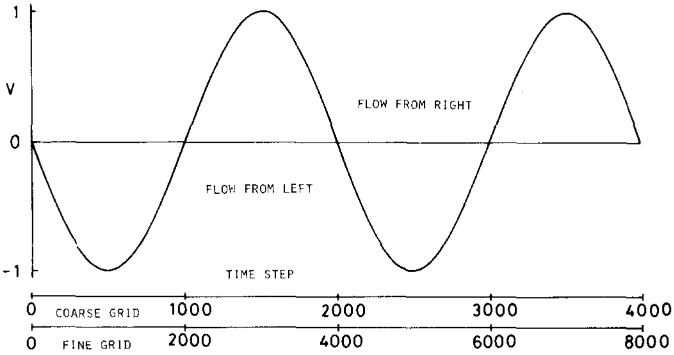

FIG. 5. Oscillation of flow velocity

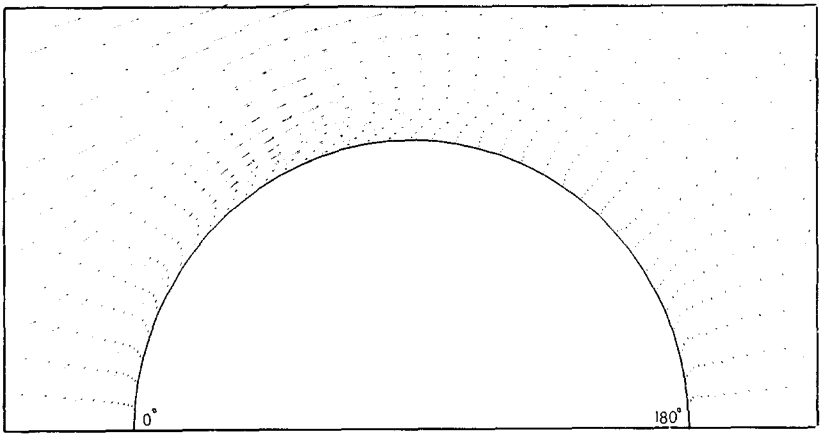

FIG. 6. Velocity vector field of a secondary twin vortex on a circular cylinder advancing steadily, Re = 1000.

The distribution of vorticity ω^3 on the cylinder surface is compared with the computation by Loc [8] in Fig. 7. It is noted that the overall agreement is good but that discrepancy still remains. This discrepancy is supposed to be due to the difference of the method of accelerating the cylinder, which determines the vorticity development. Pressure distribution at the same moment with Fig. 6 is compared with the computation at Re = 100, the computation at Re = 2000 by Kawamura and Kuwahara [7] and the measurement at Re = 2800 by Goldstein [3] in Fig. 8. Although some discrepancy is noted between computation and measurement, the degree of accuracy of the present method is supposed to be appropriate, considering that there are some differences in the Reynolds number and in the selected time level.

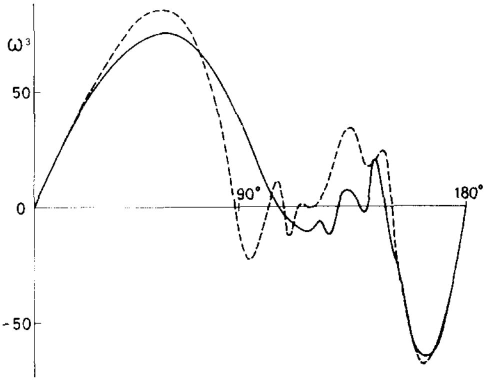

FIG. 7. Distribution of vorticity ω^3 on a circular cylinder advancing steadily at Re = 1000, $t = 2$, (–); present method (---); computation by Loc [8].

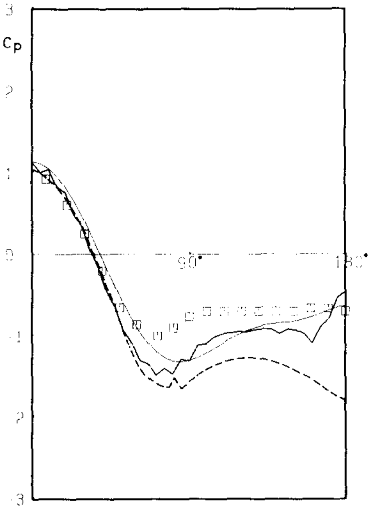

FIG. 8. Pressure distribution on a circular cylinder advancing steadily, (—); present method at Re = 1000, (-); *do* at Re = 100, □; measured at Re = 2800, from Goldstein [3], (---); computed by Kawamura and Kuwahara at Re = 2000 [7].

7.3. *Circular Cylinder in an Oscillatory Flow*

Two velocity vector fields by compact differencing and centered differencing are compared in Fig. 9 at the 2250th time-step of the flow simulation at $Kc = 5$ and Re = 1000, at which the gradually accelerating flow is incoming from right after the cylinder undergoes vortex shedding first to the left side and second to the right.

It is obviously noted that the vortical flows, on the right-hand side, above the cylinder and at the separating point on the body surface, are more clearly realized by the compact differencing method. Furthermore, the unrealistic velocity fluctuation near the body surface is removed by this higher-order accurate scheme. The pressure distribution at the same instance with Fig. 9 is compared in Fig. 10. The difference is noticeable and unrealistic fluctuation seems to be removed by the higher resolution property of the compact difference scheme.

It may be concluded that the truncation error of the centered differencing scheme contaminates the solution of this problem in a coarser grid system but that the compact difference scheme can resolve this problem with its higher-order accurate property.

8. SIMULATED VORTEX GENERATION IN AN OSCILLATORY FLOW

8.1. *Condition of Computation*

The motions of vortices around a circular cylinder in relative sinusoidal flow are very complicated and the pattern of vortex shedding varies depending on the *Kc*

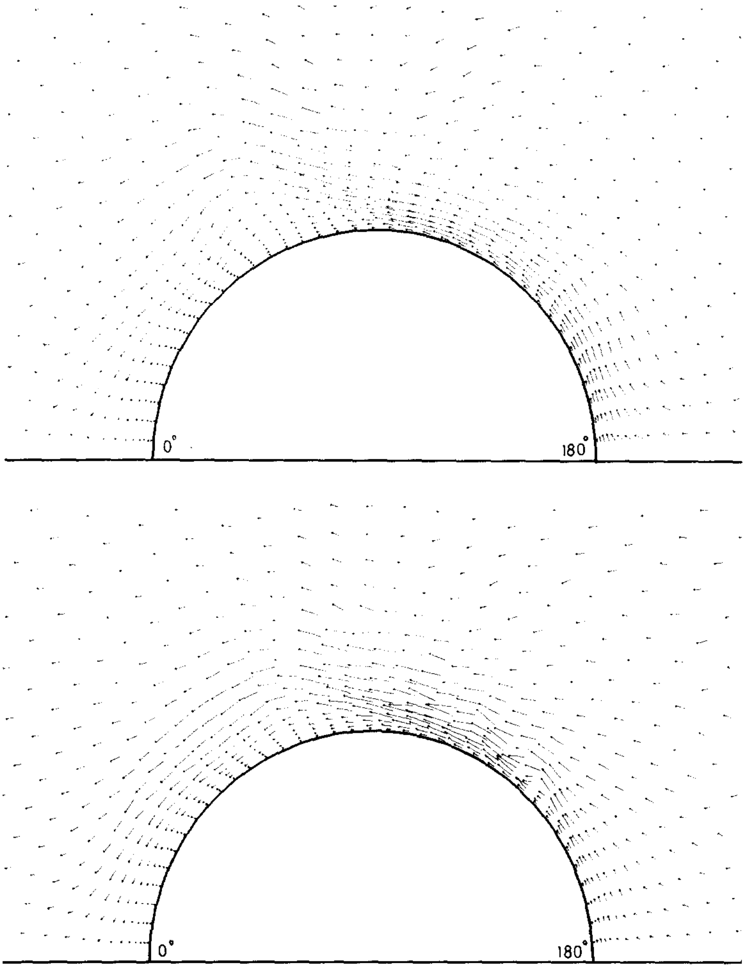

FIG. 9. Comparison of velocity vector field at $N = 2250$ ($t = 1.125$) of the case of $Kc = 5$ simulated in the coarser grid system, compact differencing (above) and centered differencing (below).

number. The pairing process of vortices from the previous half cycle with those in the present half cycle is fundamental in this oscillatory flow problem. According to Williamson [19] pairing of attached vortices is observed in the range of $Kc < 7$ as illustrated in Fig. 11. A pair of small attached vortices form in the wake of the cylinder in each half cycle and when the cylinder reverses direction they split up and pair with new vortices being finally convected away.

Two Kc numbers 5 and 7 are chosen in this section for the simulation to numerically elucidate this complicated vortex generation, shedding and pairing. The finer grid system shown in Fig. 4 is used in the computations. The number of grid

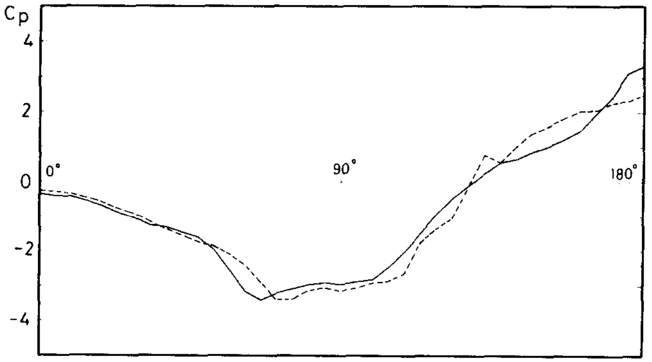

FIG. 10. Comparison of pressure distribution on the circular cylinder in the condition of Fig. 8, (–); compact differencing, (---); centered differencing.

points is $118 \times 117 \times 3$ in radial, circumferential and axial directions, respectively. Since the coordinate surfaces are attracted toward the cylinder with factors $A = 10^5$ and $B = 0.6$, the smallest spacing in the radial direction is 0.15 percent of the diameter of the cylinder. Since the amplitude of oscillation of the cylinder is $Kc \cdot d/2\pi$, the shedded vortices are not expected to go across the open boundary of the computational domain.

From the stability requirement with respect to the Courant number the time increment must satisfy the following condition, when we assume that the radial velocity is unity on the cylinder surface

$$\Delta t \leqslant \frac{0.0015}{Kc}. \tag{8.1}$$

The dimensionless time increment is set at 0.00025 for the both cases of $Kc = 5$ and 7. Therefore 4000 time-steps are required for one cycle of flow oscillation. The computation is continued for about 7000 time-steps.

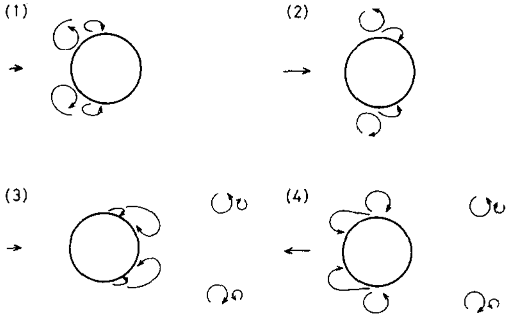

FIG. 11. Sketch of observed pairing of attached vortices for $Kc < 4$, arrows refer to the flow direction.

In the present problem of vortex shedding the solution often starts to show fluctuations in the region of shed vortices apart from the cylinder, where the grid system is relatively coarser. This determines the uppermost value of Reynolds number. It is 1000 for the case of $Kc = 5$, but it is reduced to 700 for the case of $Kc = 7$, since the vortices are shed farther away from the cylinder with the increasing Kc number.

8.2. $Kc = 5$

Velocity vector fields, contour maps of in-line velocity u^1, transverse velocity u^2, pressure P and vorticity with the axis parallel to the axis of the cylinder ω^3 are shown in Figs. 12–16, respectively. Figures 12, 15, and 16 contain 6 frames from $N = 4000$ to 6500 with the interval of 500 time-steps. The first cycle of flow oscillation is ceased and a new flow from right starts to come in at $N = 4000$, when the cylinder is just started to move to the right. The former half of the second cycle is ceased at $N = 6000$ as shown in Fig. 5. In the contours of velocities u^1 is taken to be positive when it is directed to the right and u^2 when it is directed upward.

The boundary layer on the cylinder seems to be resolved by the present grid system and very complicated distortion of fluid flow on the top (90°) of the cylinder is noticeable. This is presumably due to the pairing with the vortex of opposite sign that is generated in the previous half cycle. Since these velocity vector fields are shown in a reference frame fixed to the cylinder, contrary to the flow visualization by Williamson [19], the vortices surrounding and affecting on the flow along the surface of the cylinder are not clearly observed. However, the contour maps are effective for the visualization of the complicated mechanism of vortex shedding and for the quantitative understanding of the physical values.

The contours of in-line velocity u^1 in Fig. 13 show that a complicated velocity field is present at $V = 0.0$ ($N = 4000$) owing to the vortex shedding of the previous cycle. At the next stage of $N = 4500$ the contours are remarkably distorted with the contour of highest value being split up. The maximum value of u^1 is 2.6 times larger than the flow velocity at infinity at the moment when the flow velocity is maximum at $N = 5000$.

At $N = 4000$ in the contour map of the transverse velocity u^2 in Fig. 14, when the velocity of the oscillation is zero, u^2 takes very high value $1 \cdot 2$. The twin vortices generated in the previous half cycle cause very high transverse velocity near the cylinder surface and this seems to accelerate the flow separation. The u^2 field at $N = 6500$ is not completely asymmetric to that of $N = 4500$ presumably due to the difference of the repeated number of cycle.

The contour map of pressure P, which has the same magnitude with pressure coefficient, is shown in Fig. 15. The lowest pressure contour of -4 is observed at $N = 4500$ when the flow distortion causes remarkable separation.

The contour maps of vorticity ω^3 are shown in Fig. 16 and more detailed ones are also shown in Fig. 17 with the smaller interval of 250 steps. These figures are most suitable for the understanding of the mechanism of vortex shedding. At the

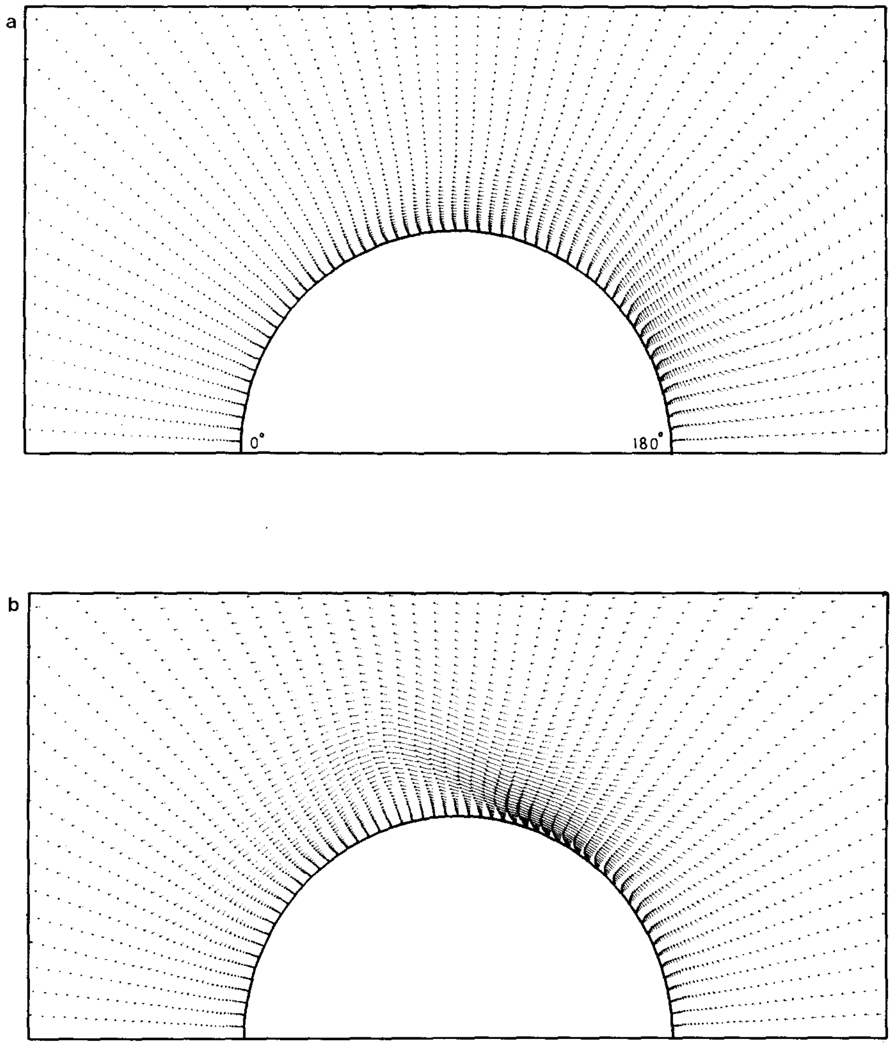

FIG. 12. Velocity vector field for the case of $Kc = 5$ and $\mathrm{Re} = 1000$, (a) $N = 4000$, $t = 1.000$, $V = 0.00$; b) $N = 4500$, $t = 1.125$, $V = -0.71$.

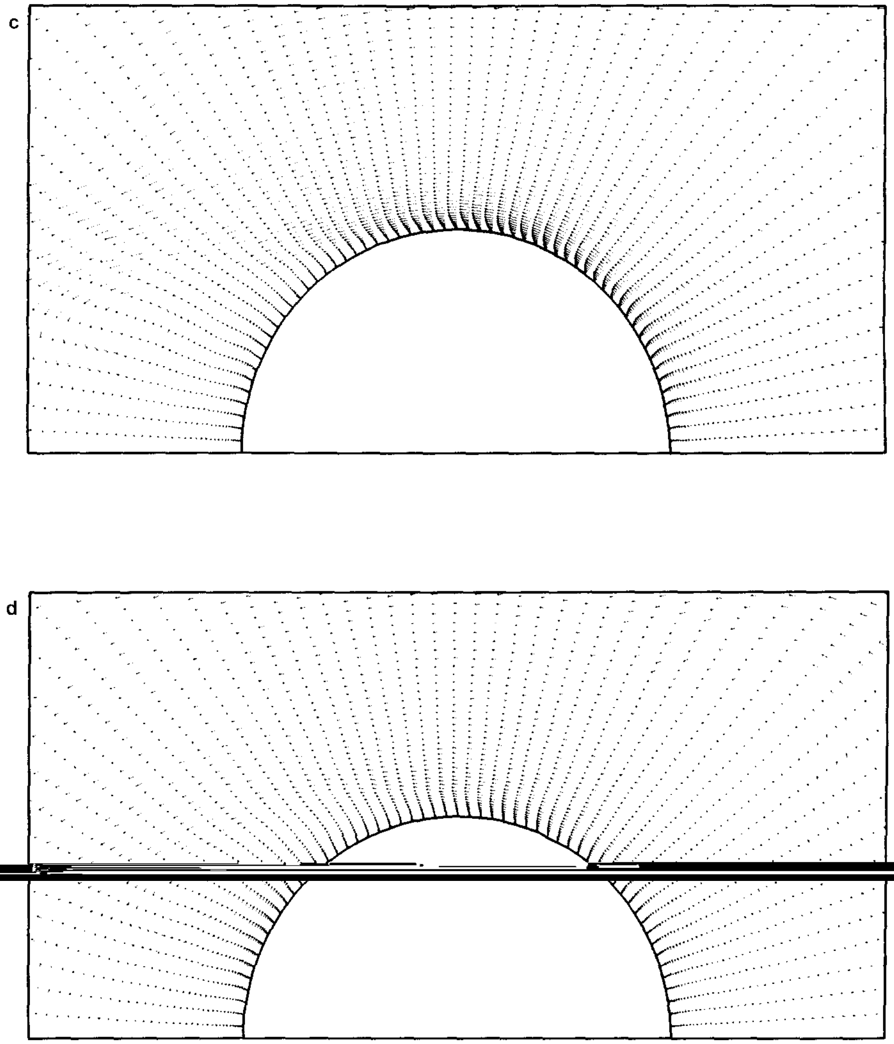

FIG. 12 (*continued*). (c) $N = 5000$, $t = 1.250$, $V = -1.00$; (d) $N = 5500$, $t = 1.375$, $V = -0.71$.

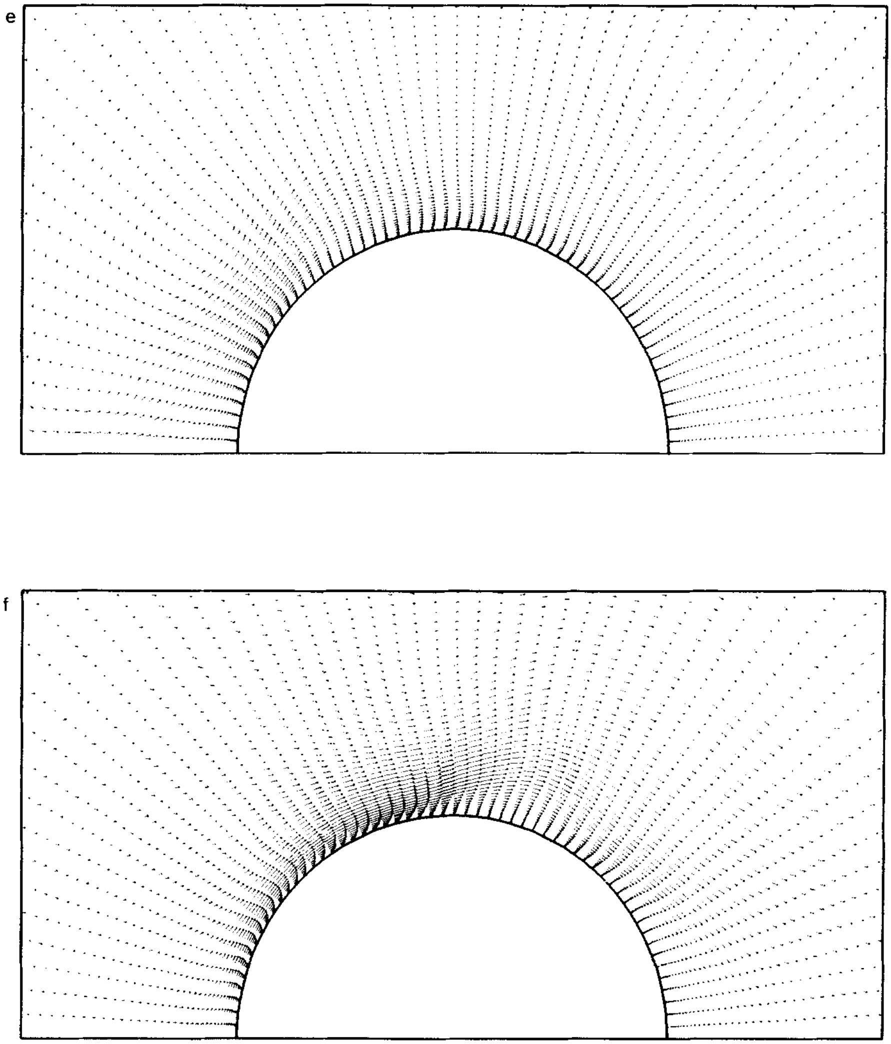

FIG. 12 (*continued*). (e) $N = 6000$, $t = 1.500$, $V = 0.00$; (f) $N = 6500$, $t = 1.625$, $V = 0.71$.

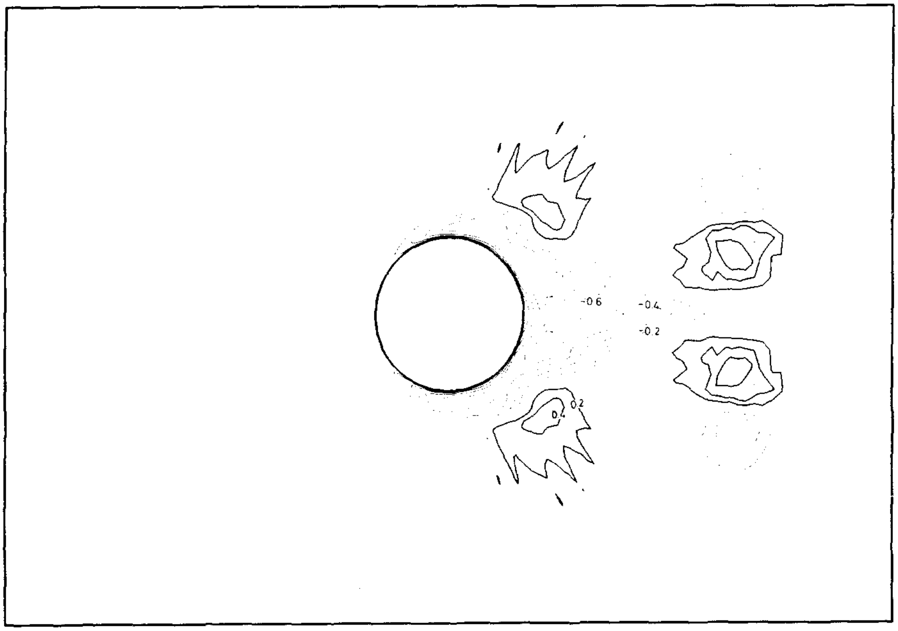

FIG. 13. Contour map of velocity u^1 for the case of $Kc = 5$ and $\mathrm{Re} = 1000$, the contour interval is 0.2 and contours of positive values are drawn in bold lines, $N = 4000$, $t = 1.000$, $V = 0.00$.

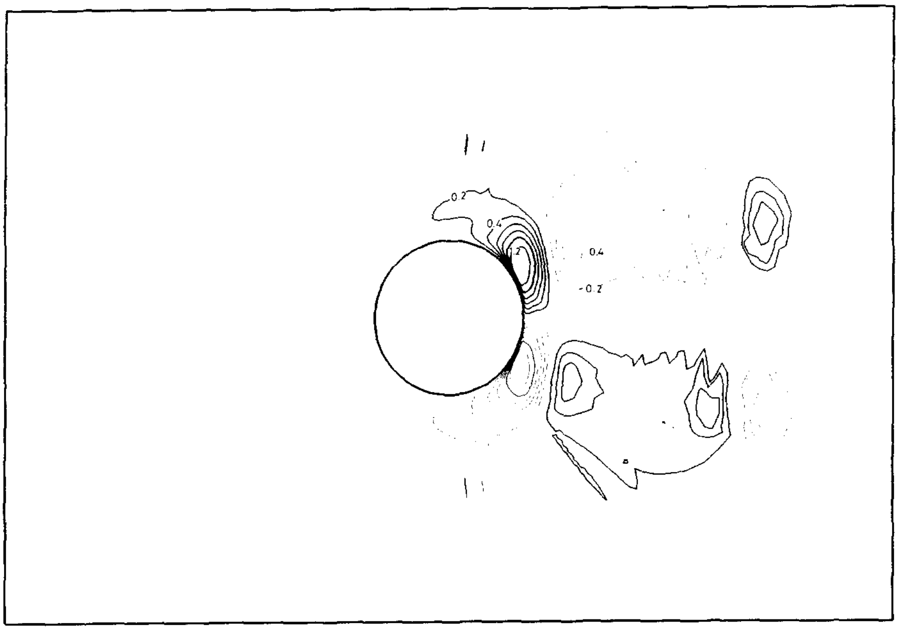

FIG. 14. Contour map of velocity u^2 for the case of $Kc = 5$ and $\mathrm{Re} = 1000$, the contour interval is 0.2 and contours of positive values are drawn in bold lines, $N = 4000$, $t = 1.000$, $V = 0.00$.

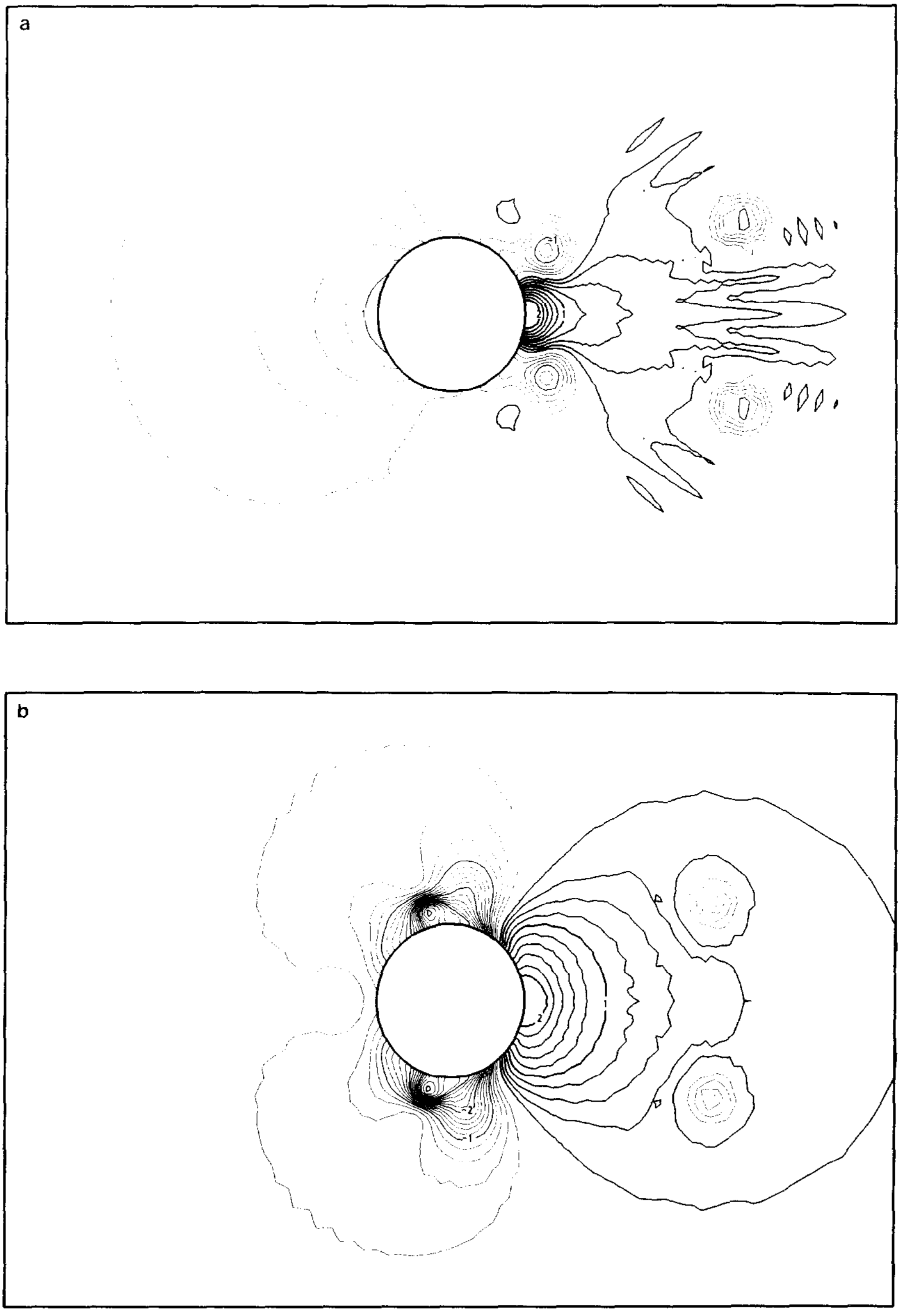

FIG. 15. Contour map of pressure P for the case of $Kc = 5$ and $\mathrm{Re} = 1000$, the contour interval is 0.2 and contours of positive values are drawn in bold lines, (a) $N = 4000$, $t = 1.000$, $V = 0.00$; (b) $N = 4500$, $t = 1.125$, $V = -0.71$.

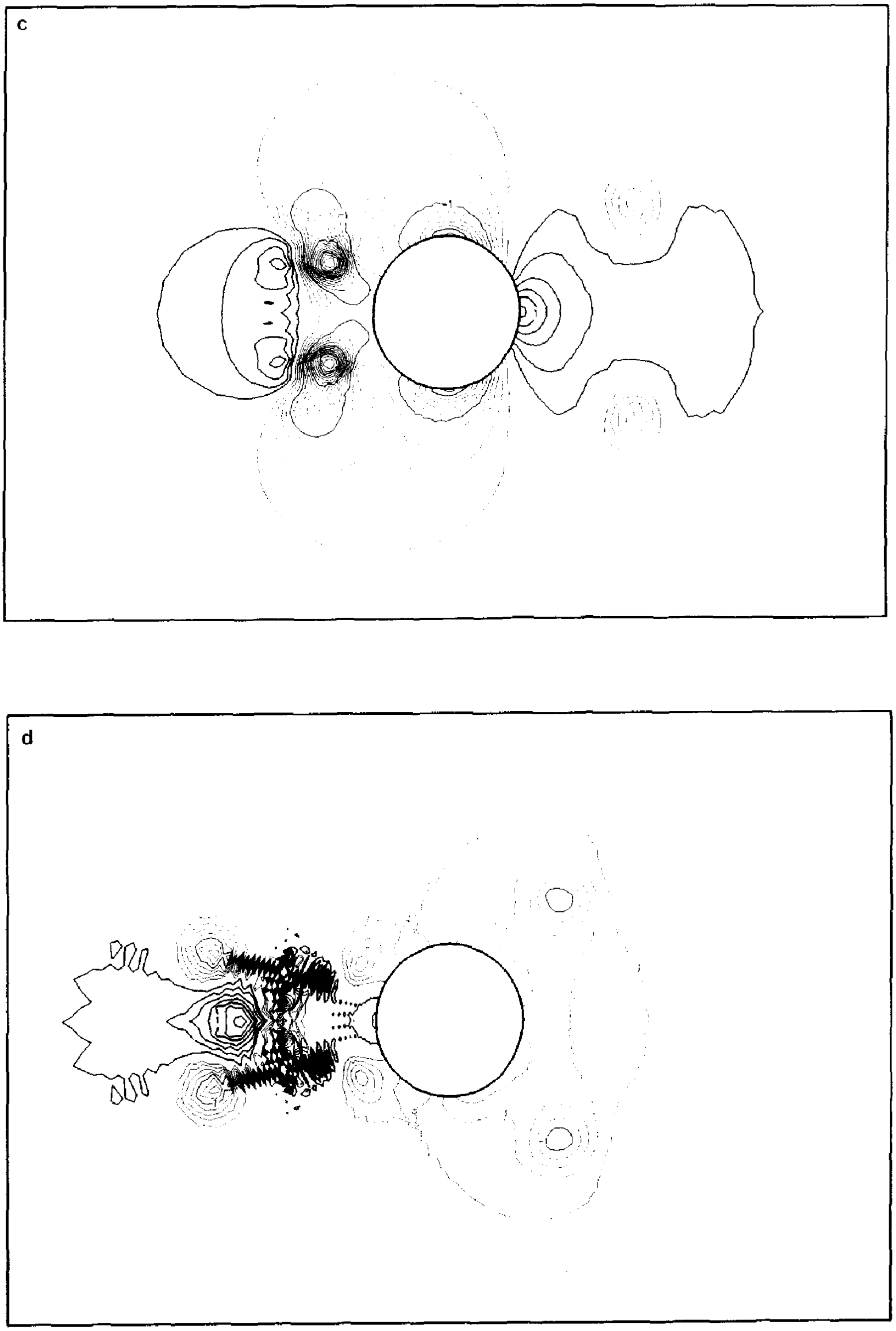

FIG. 15 (*continued*). (c) $N = 5000$, $t = 1.250$, $V = -1.00$; (d) $N = 5500$, $t = 1.375$, $V = -0.71$.

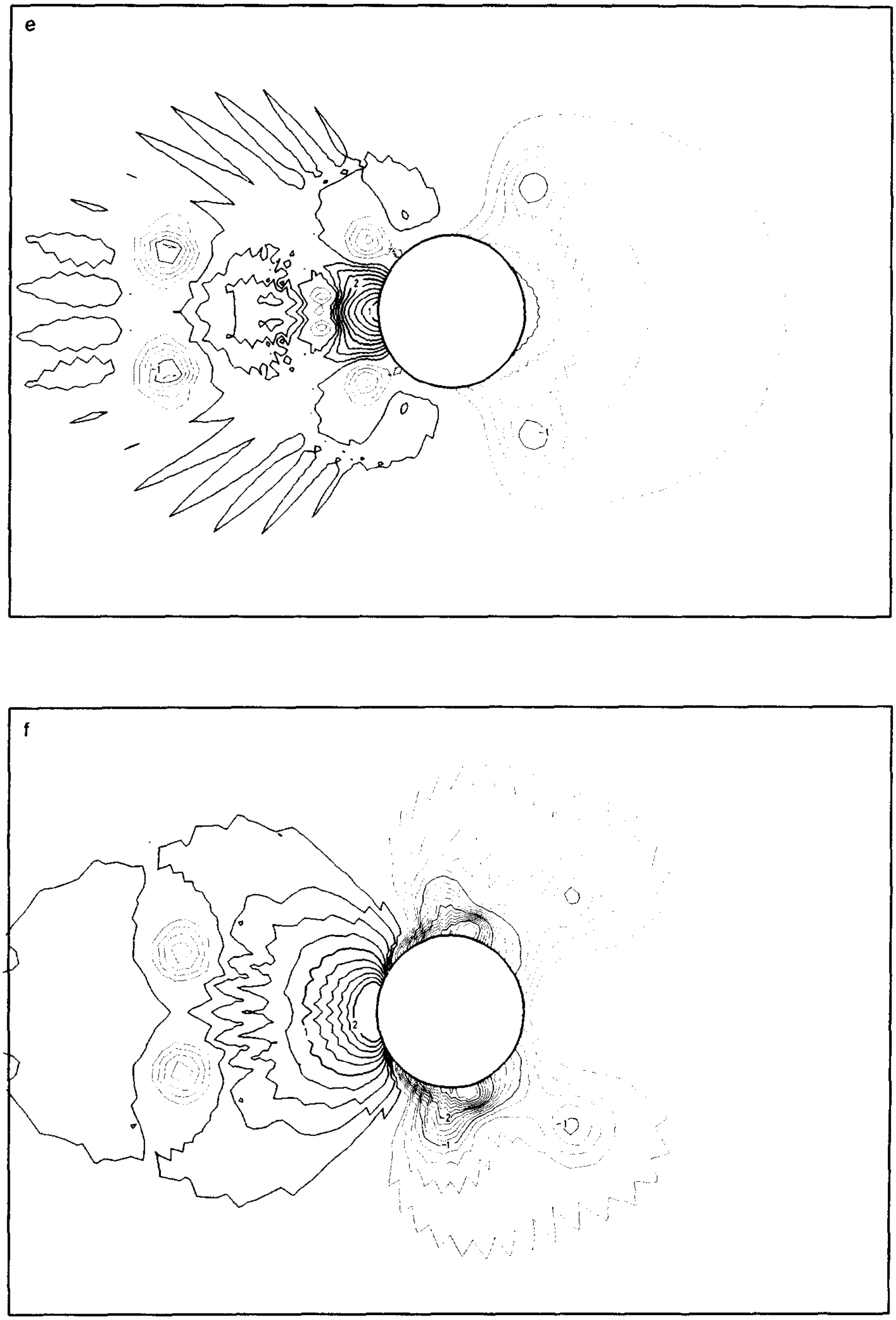

FIG. 15 (*continued*). (e) $N=6000$, $t=1.500$, $V=0.00$; (f) $N=6500$, $t=1.625$, $V=0.71$.

moment of $N = 4000$ when the cylinder just starts to move to the right, the upper surface of the cylinder is already covered with vorticity of anticlockwise rotation owing to the vortex motion of the previous half cycle. This vorticity layer starts to be split up and separated at the point around 120° at $N = 4250$. Then, this separating motion leads to shedding of vortices at $N = 4750$ when the oscillation speed approaches close to the maximum value and at this moment vorticity layer of opposite sign appears on the left hand surface of the cylinder. The pairing of the vortex generated in this half cycle with one generated in the previous half cycle is very interesting. The new vortex is separated into two; one is attached to the cylinder and the other is shedded to the left together with the vortex of the previous half cycle. Pairing of attached vortices and that of shed vortices are both present, which seems to be a particular property of vortex shedding at this low Kc number. The fluctuation of flow variables appears where the vortex generated in this half cycle is convected away to the far field with the vorticity of large magnitude. This is due to the inadequate spatial resolution of the present method, since the grid spacing becomes coarser with the increase of distance from the cylinder. The vortex influenced by this fluctuation gradually comes back to the surface of the cylinder and disappears at $N = 6500$, which is one of the most noticeable point that differs from the experiment by Williamson illustrated in Fig. 11, in which the shed vortex does not come back to the cylinder but it shows more intimate pairing motion away from the cylinder. This difference is mostly attributable to the difference of both Kc and Re numbers and partly to the fluctuation of flow field due to the inadequate resolution of the computational method which dissipates the energy of the shed vortex that may interact with the vortex of the previous half cycle with opposite sign more intimately.

The pressure distribution on the cylinder surface is shown in Fig. 18. The positive value exceeds 3 and the negative one -3, and the variation of distribution is very abrupt and complicated. It seems to be difficult to find similarity with the pressure distribution in steady motion.

8.3. $Kc = 7$

Contour maps of vorticity are shown in Fig. 19 for the case of $Kc = 7$. The overall pattern of vortex shedding is similar to the case of $Kc = 5$. Unsymmetric vortex shedding does not yet appear, but the flow is completely symmetric in this simulation. However, the fluid motion is much more dynamic, since the amplitude of the oscillation is larger than the case of $Kc = 5$ by 40 percent. The vortex caused by the splitting up motion is moved upward and backward and shedded farther by the large amplitude of oscillation. Two pairs of shed vortices and two pairs of attached vortices are present after the velocity begins to decrease at $N = 5000$. The distance of shed vortices from the cylinder is farther in proportion to the Kc number and the shed vortex generated in the present half cycle does not come back to the body surface contrary to the case of $Kc = 5$.

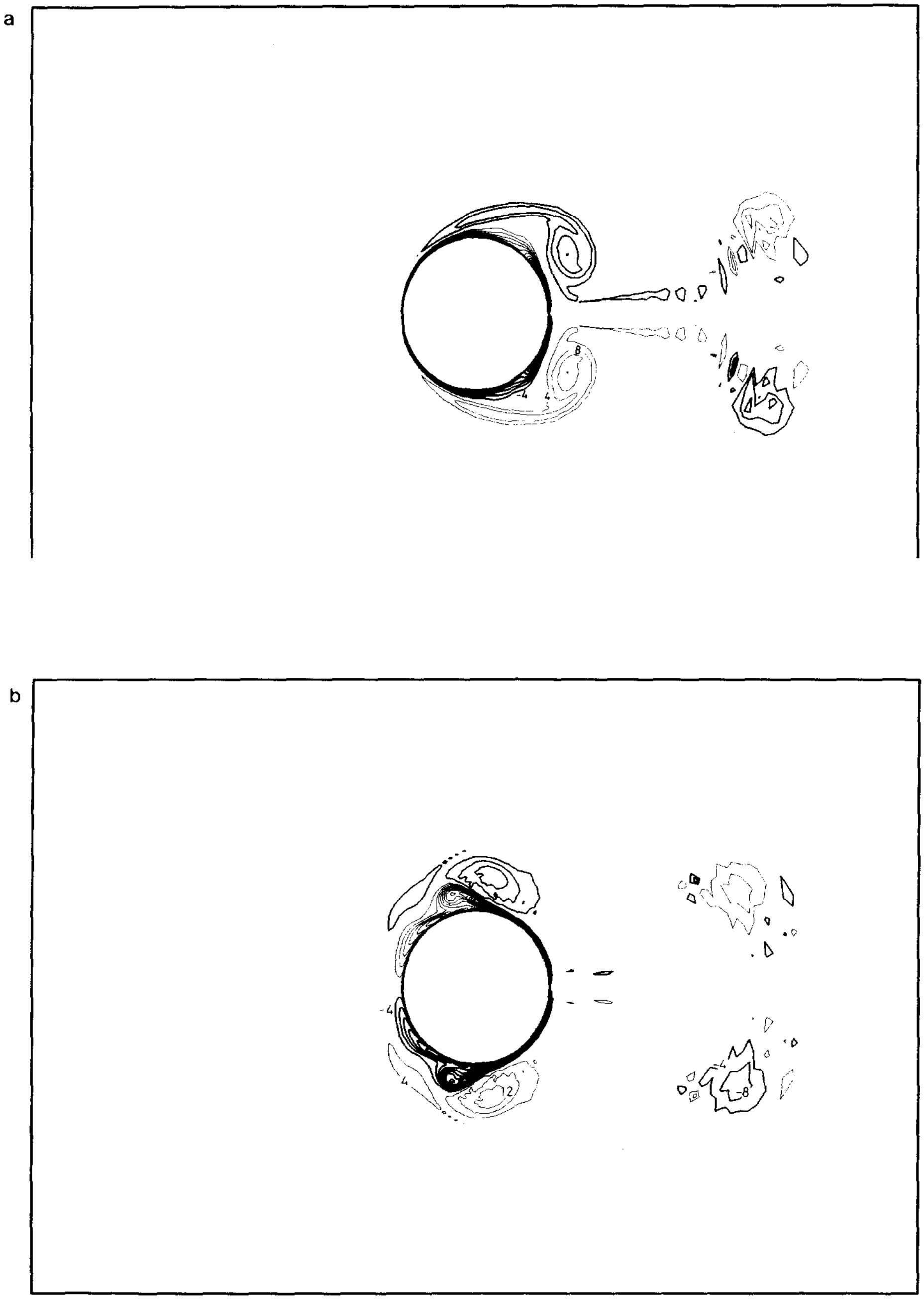

FIG. 16. Contour map of vorticity ω^3 for the case of $Kc = 5$ and $\mathrm{Re} = 1000$, the contour interval is 4 and contours of clockwise rotation are drawn in bold lines, (a) $N = 4000$, $t = 1.000$, $V = 0.00$; (b) $N = 4500$, $t = 1.125$, $V = -0.71$.

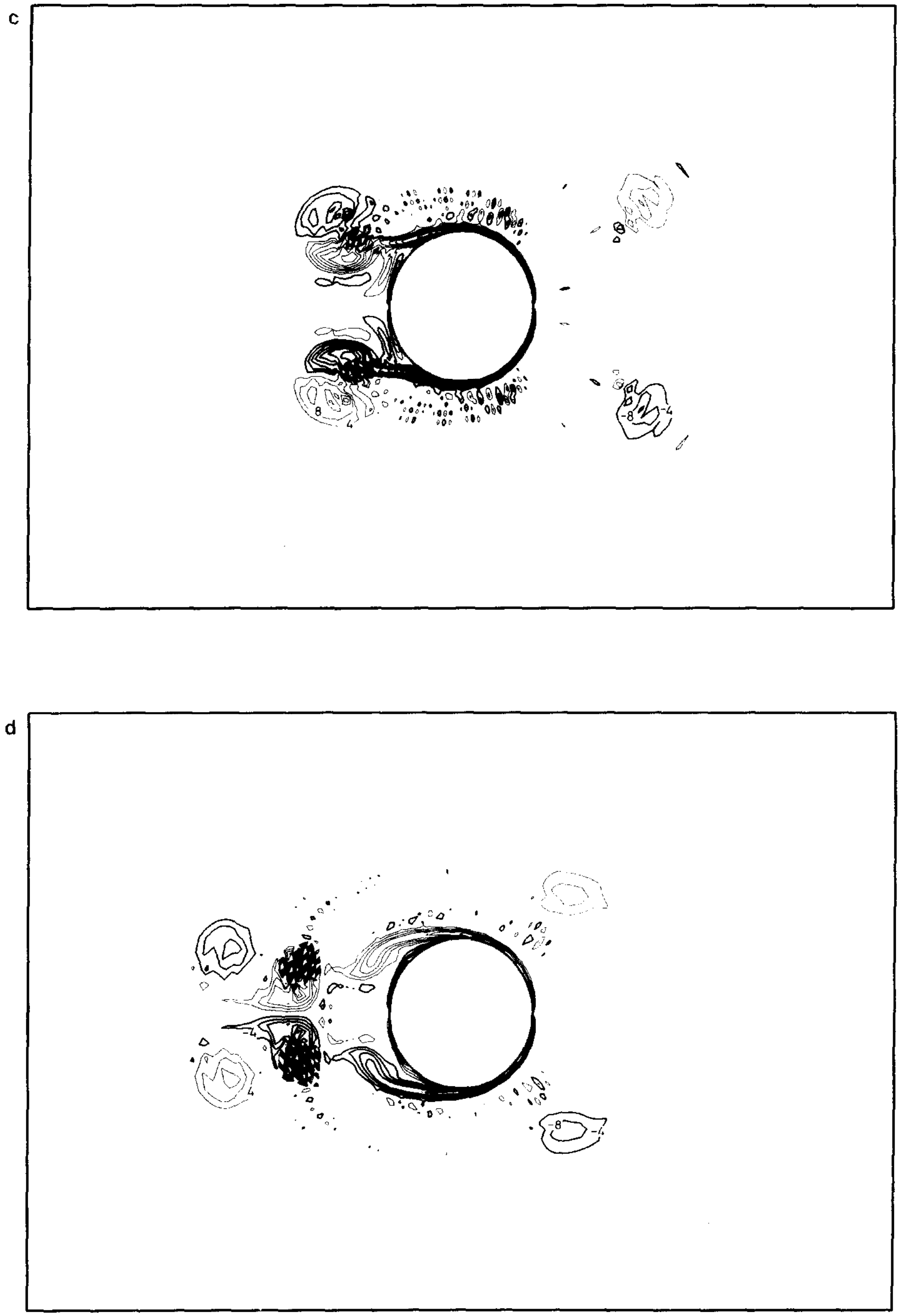

FIG. 16 (*continued*). (c) $N = 5000$, $t = 1.250$, $V = -1.00$; (d) $N = 5500$, $t = 1.375$, $V = -0.71$.

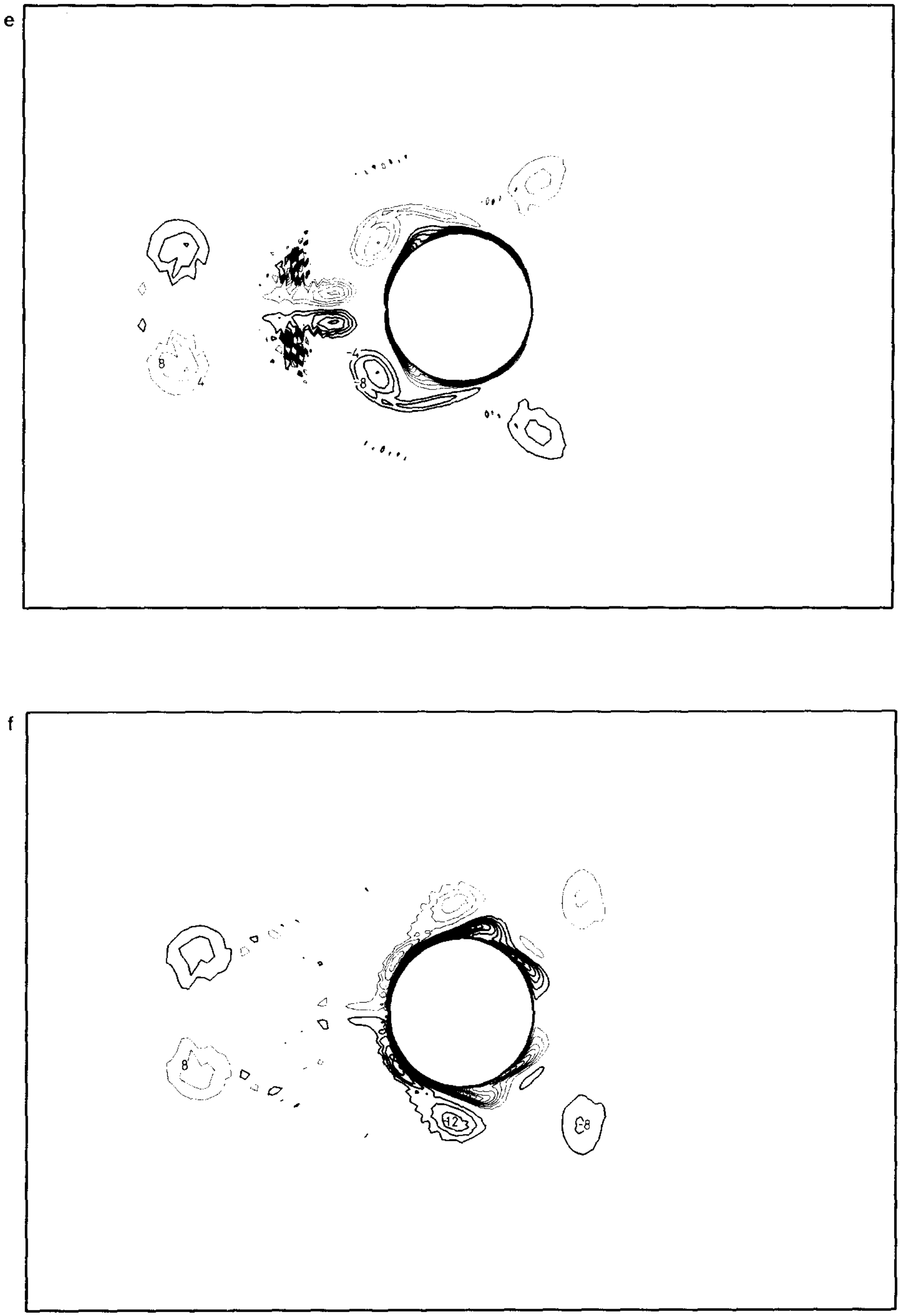

FIG. 16 (*continued*). (e) $N = 6000$, $t = 1.500$, $V = 0.00$; (f) $N = 6500$, $t = 1.625$, $V = 0.71$.

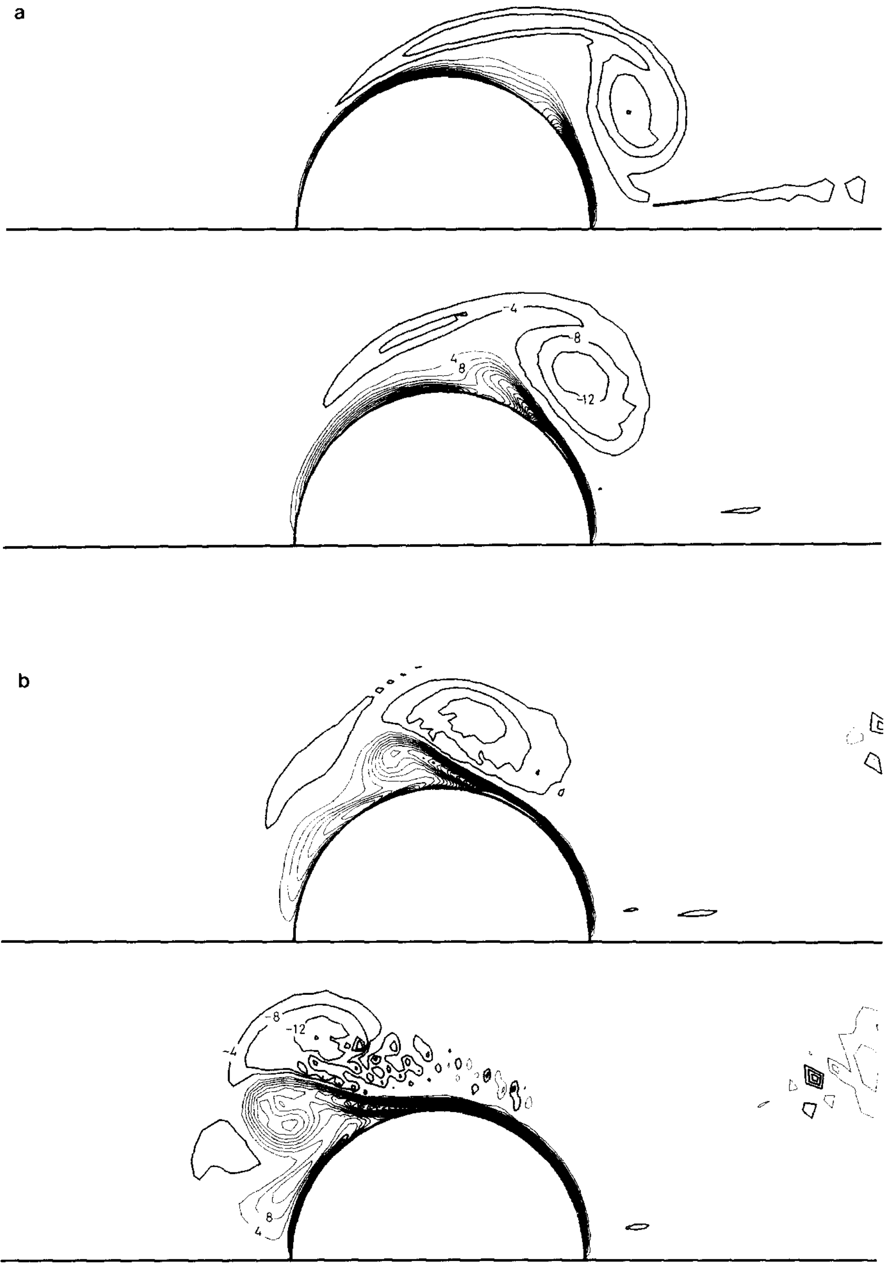

FIG. 17. Detailed contour map of vorticity ω^3 for the case of $Kc = 5$ and $\mathrm{Re} = 1000$, the contour interval is 4 and contours of clockwise rotation are drawn in bold lines, (a) $N = 4000$, $t = 1.000$, $V = 0.00$ and $N = 4250$, $t = 1.063$, $V = -0.38$; (b) $N = 4500$, $t = 1.125$, $V = -0.71$ and $N = 4750$, $t = 1.188$ $V = -0.92$.

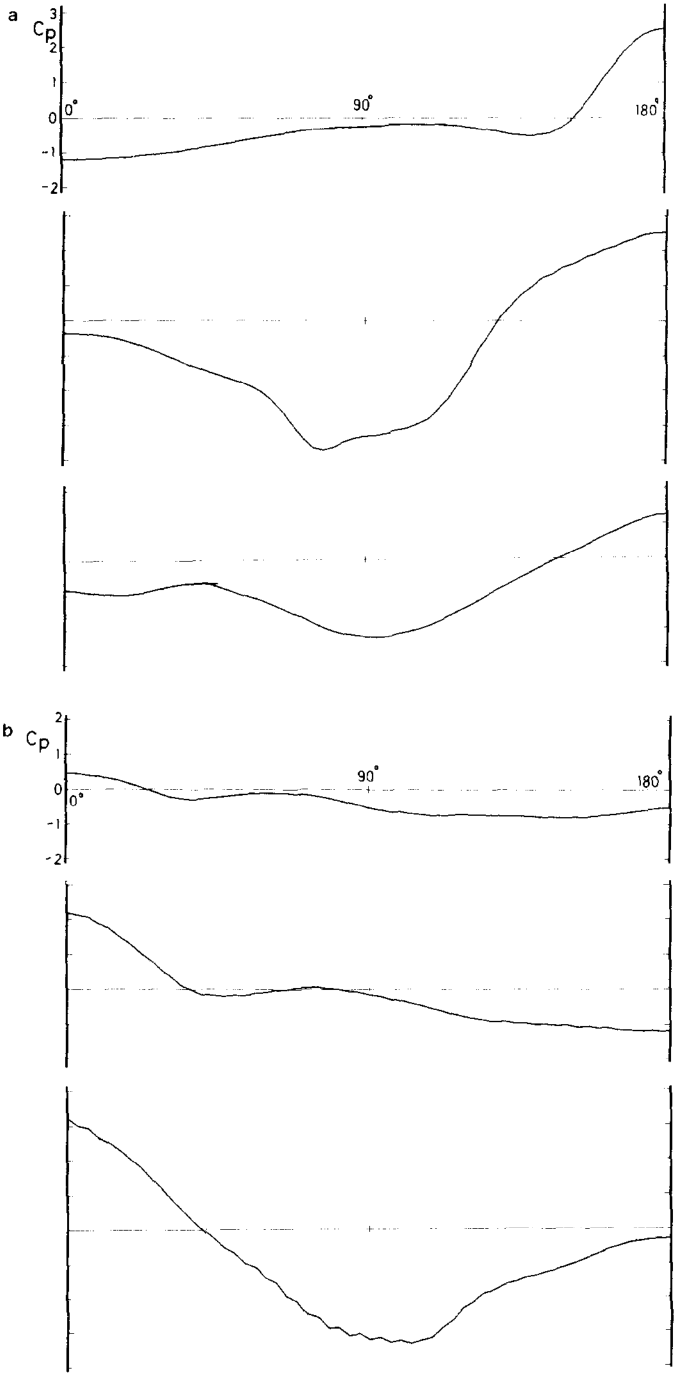

FIG. 18. Pressure distribution on body surface for the case of $Kc = 5$ and $\mathrm{Re} = 1000$, (a) $N = 4000$, 4500, and 5000; (b) $N = 5500$, 6000, and 6500.

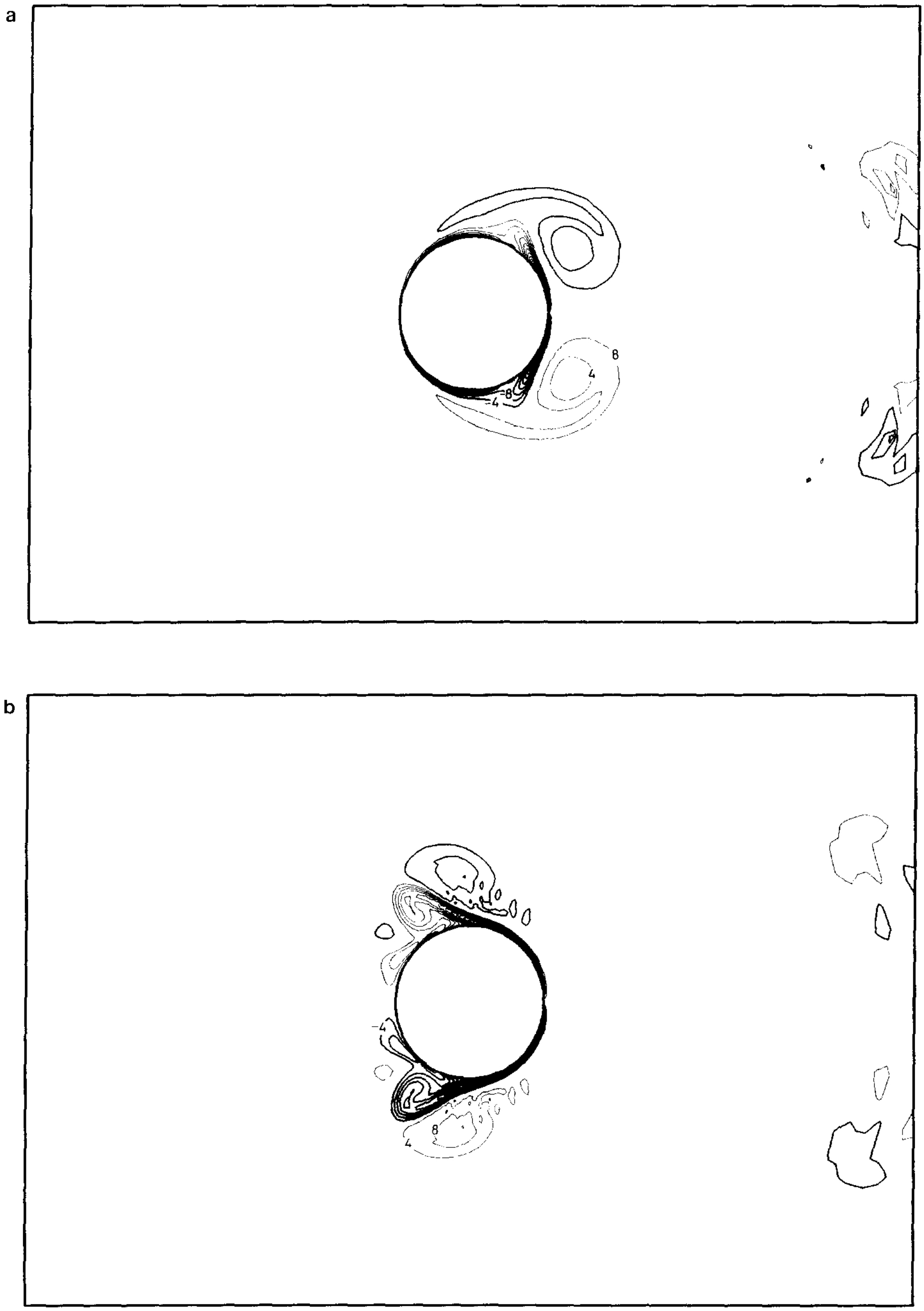

FIG. 19. Contour map of vorticity ω^3 for the case of $Kc = 7$ and $\mathrm{Re} = 700$, the contour interval is 4 and contours of clockwise rotation are drawn in bold lines, (a) $N = 4000$, $t = 1.000$, $V = 0.00$; (b) $N = 4500$, $t = 1.125$, $V = -0.71$.

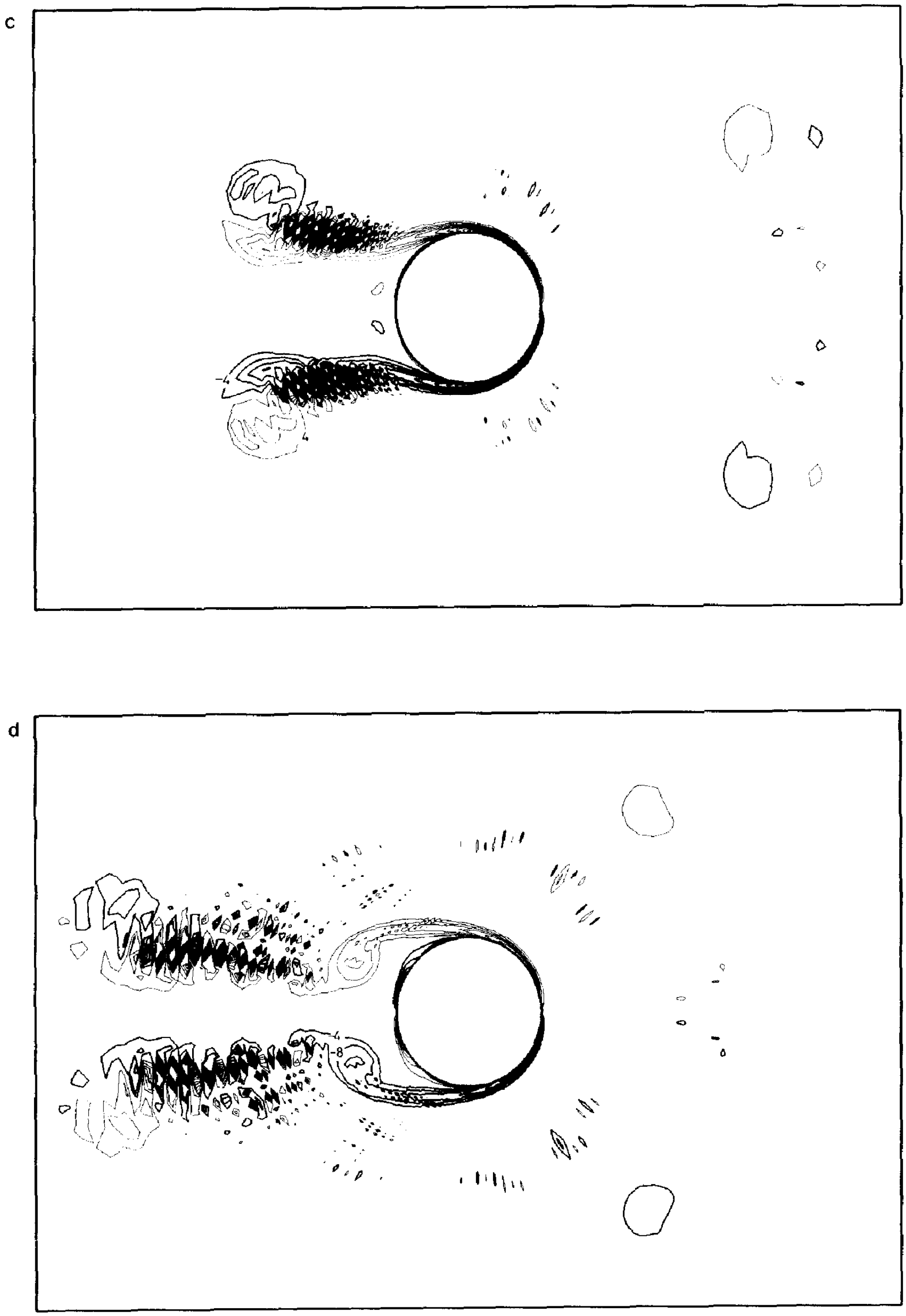

FIG. 19 (*continued*). (c) $N=5000$, $t=1.250$, $V=-1.00$; (d) $N=5500$, $t=1.375$, $V=-0.71$.

e

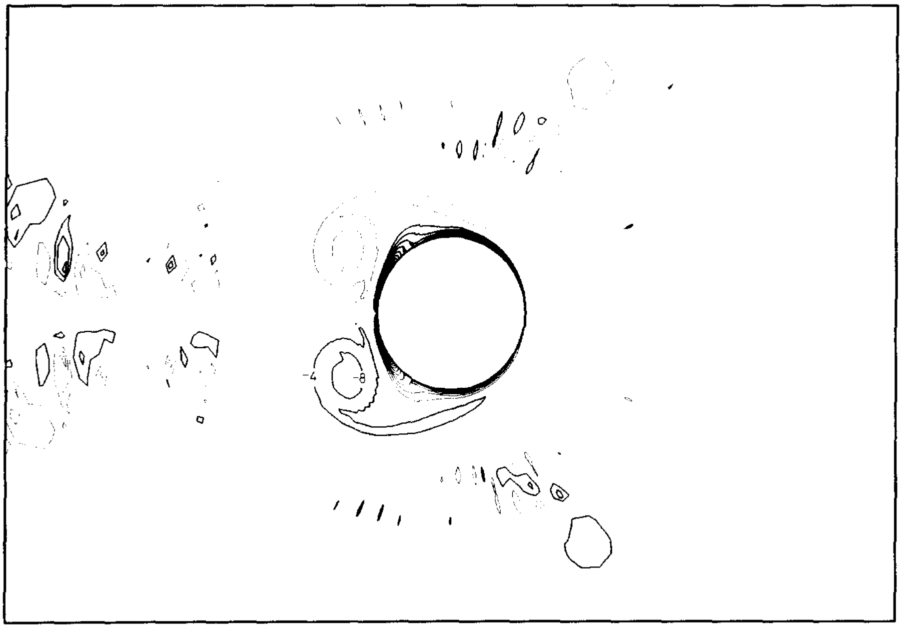

f

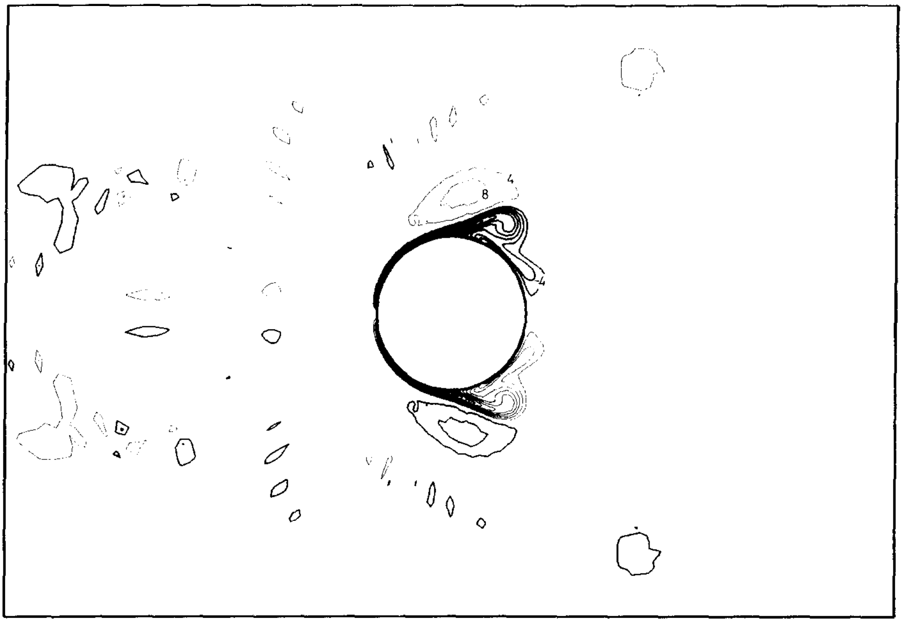

FIG. 19 (*continued*). (e) $N = 6000$, $t = 1.500$, $V = 0.00$; (f) $N = 6500$, $t = 1.625$, $V = 0.71$.

8.4. *Discussion*

At relatively low *Kc* number the process from flow separation to vortex shedding is very complicated, since the vortices generated in the previous cycles are present near the cylinder and they are very influential to the succeeding flow separation. The present method of directly integrating the NS-equation with high degree of accuracy seems to be very useful for the elucidation of the details of the complicated flow mechanism, to which both experimental approaches with various instruments and numerical approaches with various postulations to simplify the problem, such as a discrete vortex modelling, will find serious difficulties.

The computations were performed by a super-computer HITAC S-810/20 of which top speed is about 650 MFLOPS. The CPU time required by the computation of 7000 time-steps was about 10 h by the scalar processor and about 4 h by the vector processor, since the number of iteration for the solution of (4.3) sometimes approaches 300 when the change of the flow field is abrupt. Although almost all parts of the computer code is vectorized, it seems to leave room for improvement.

9. Concluding Remarks

A higher-order accurate difference method for a viscous flow was developed. The simulated example of vortex shedding from a circular cylinder in an oscillatory flow at low *Kc* number elucidated the complicated vortex generation, separation and pairing motions. It seems to be demonstrated that the present method is a useful tool of numerical experiments to derive sound understanding of the detailed viscous flow mechanics. Since the formulation and the computer code are written in three [redacted] the present method requires a very fine grid system and gives a serious limitation on diffusion number, which leads to high cost of numerical experiments. A proper turbulence model must be introduced for the simulation of a higher Reynolds number flow. These must be considered in future.

Acknowledgments

The computations were performed by the super-computer HITAC S-810/20 of the Computer Centre, the University of Tokyo. The authors express a lot of thanks to Professor Kajitani and other colleagues at the Experimental Tank of the University of Tokyo for their interest and assistance. This research is partly supported by the Grant-in-Aid for Cooperative Research of the Ministry of Education, Science and Culture.

REFERENCES

1. H. M. BADR AND S. C. R. DENNIS, *J. Fluid Mech.* **158**, 447 (1985).
2. I. CHRISTIE, *J. Comput. Phys.* **59**, 353 (1983).
3. S. GOLDSTEIN, *Modern Developments in Fluid Dynamics* (Oxford Univ. Press, London, 1938).
4. F. H. HARLOW AND J. E. WELCH, *Phys. Fluids* **8**, 2182 (1965).
5. R. S. HIRSH, *J. Comput. Phys.* **19**, 90 (1975).
6. H. HONJI AND S. TANEDA, *J. Phys. Soc. Jpn.* **27**, 1668 (1969).
7. T. KAWAMURA AND K. KUWAHARA, AIAA paper 84-0340, 1984 (unpublished).
8. T. P. LOC, *J. Fluid Mech.* **100**, 111 (1980).
9. C. W. MASTIN AND J. F. THOMPSON, *Numer. Math.* **29**, 397 (1978).
10. N. N. MAUSOUR, P. MOIN, AND W. C. REYNOLDS, in *Turbulent Shear Flow I*, F. Durst *et al.*, (Springer, Berlin, 1979).
11. H. MIYATA, S. NISHIMURA, AND A. MASUKO, *J. Comput. Phys.* **60**, 3, 391 (1985).
12. H. MIYATA, S. NISHIMURA AND H. KAJITANI, in *Proceedings of the 4th Intern. Conf. on Numerical Ship Hydrodynamics, Washington D.C., 1985*, edited by J. McCarthy *et al.*, (David Taylor Naval Ship R&D Center, 1985).
13. S. A. ORSZAG AND M. ISRAELI, *Ann. Rev. Fluid Mech.* **6**, 281 (1974).
14. T. SARPKAYA AND M. ISAACSON, *Mechanics of Wave Forces on Offshore Structures* (Van Nostrand–Reinhold, Melbourne, 1981).
15. S. P. SHANKS AND J. F. THOMPSON, in *Proceedings of the 2nd Intern. Conf. on Numerical Ship Hydrodynamics, Berkeley, 1977*, edited by J. V. Wehausen and N. Salvesen (David Taylor Naval Ship R&D Center, 1977).
16. J. F. THOMPSON, F. C. THAMES, AND C. W. MASTIN, *J. Comput. Phys.* **15**, 299 (1974).
17. J. F. THOMPSON AND Z. U. A. WARSI, *J. Comput. Phys.* **47**, 1 (1982).
18. Z. U. A. WARSI, *AIAA J.* **19**, 240 (1981).
19. C. H. K. WILLIAMSON, *J. Fluid Mech.* **155**, 141 (1985).